ACS APPLIED ENERGY MATERIALS

www.acsaem.org Letter

Synchrotron Imaging of Pore Formation in Li Metal Solid-State Batteries Aided by Machine Learning

Marm B. Dixit, Ankit Verma, Wahid Zaman, Xinlin Zhong, Peter Kenesei, Jun Sang Park, Jonathan Almer, Partha P. Mukherjee, and Kelsey B. Hatzell*

Cite This: *ACS Appl. Energy Mater.* 2020, 3, 9534–9542 Read Online

ACCESS | Metrics & More | Article Recommendations | Supporting Information

ABSTRACT: High-rate capable, reversible lithium metal anodes are necessary for next generation energy storage systems. In situ tomography of Li|LLZO|Li cells is carried out to track morphological transformations in Li metal electrodes. Machine learning enables tracking the lithium metal morphology during galvanostatic cycling. Nonuniform lithium electrode kinetics are observed at both electrodes during cycling. Hot spots in lithium metal are correlated with microstructural anisotropy in LLZO. Mesoscale modeling reveals that regions with lower effective properties (transport and mechanical) are nuclei for failure. Advanced visualization combined with electrochemistry represents an important pathway toward resolving non-equilibrium effects that limit rate capabilities of solid-state batteries.

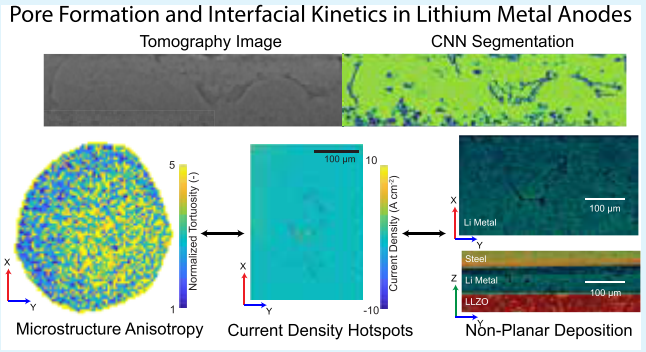

KEYWORDS: *solid electrolytes, LLZO, tomography, solid-state battery, lithium metal, machine learning*

Metal anodes (Li, Na, Mg) benefit from high specific energy because the entire electrode volume is active.[1] However, high reactivity in liquid electrolytes and non-uniform electrodeposition severely limits its application. Electrodeposition instabilities and dendrite formation in liquid binary electrolytes can occur because of transport limitations and the formation of concentration gradients at high charge rates. Prior theoretical studies have hypothesized that using a rigid solid electrolyte with a shear modulus 2× larger than that of metallic lithium could suppress lithium penetration.[2] Numerous experimental studies contradict this result[3] and demonstrate that both soft (polymers, sulfides) and hard (oxides) solid electrolytes can impact the morphological evolution of lithium metal during electrodeposition and dissolution.[4−7] Thus, a solid electrolyte's stiffness or shear modulus (G) cannot completely describe lithium filament formation and growth in solid-state batteries. Instead, unstable electrodeposition is related to chemomechanical properties at the anode|electrolyte interface that drives nonuniform Li^+ transport.

Mechanical stress at the anode|electrolyte interface impacts ion transport and reaction kinetics that govern lithium metal morphological evolution.[1,8,9] Recently, a set of chemo-mechanical design rules were proposed to achieve solid electrolytes with pressure-driven dendrite blocking or density-driven dendrite suppressing properties.[10,11,12] Spatio-temporal evolution of an electrodepositing interface can be tailored via control over the solid electrolyte's partial molar volume of Li^+ (V_{Li^+}) and shear moduli relative to lithium anode properties (V_{Li^+}/V_{Li}, G_s/G_{Li}). However, this theoretical framework assumes uniform material properties, continuous interfaces, and defect and contamination free materials. In reality, both the solid electrolyte and lithium metal contain chemical impurities and microstructure heterogenities (grains, defects, etc.) which will influence the morphological progression of the reaction interface.

Above a critical current density, Li metal morphological changes can lead to interface deterioration, contact loss, and an increase in the overpotential.[13] Recently, contact loss[14] (Figure 1a) and pore formation[15,16] in Li metal upon stripping (Figure 1a) were experimentally observed using ex situ scanning electron microscopy and in situ X-ray tomography. Pore or "void" formation upon stripping may be the origin for interface deterioration, yet there is little known about how pores form. It has been postulated that, upon Li dissolution, vacancies can form at the anode|electrolyte interface. Limited self-diffusion of lithium atoms in metallic lithium can lead to the accumulation of "voids" at high discharge currents (Figure 1b)[17] and possibly vacancy and pore gradients within the lithium metal anode.[18,19] With the exception of a few low-resolution experimental

Received: August 25, 2020
Accepted: September 14, 2020
Published: September 14, 2020

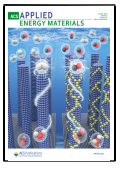

https://dx.doi.org/10.1021/acsaem.0c02053
ACS Appl. Energy Mater. 2020, 3, 9534–9542

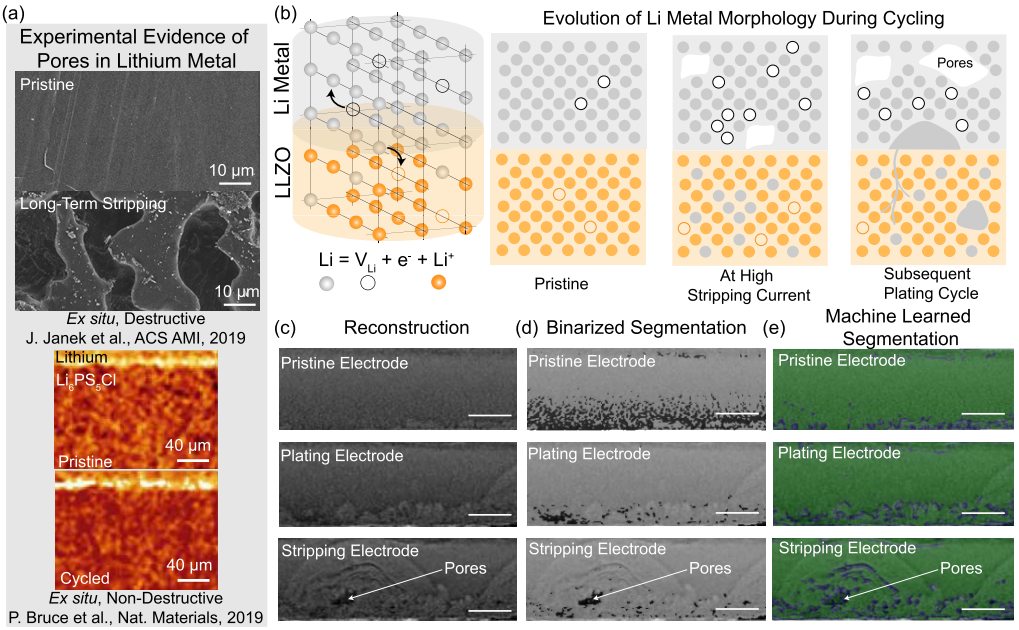

Figure 1. (a) State-of-the-art characterization for Li metal. Ex situ SEM and XRT show evidence of pore formation on Li metal after stripping. Top part adapted with permission from ref 31. Copyright 2019 American Chemical Society. Bottom part adapted with permission from ref 16. Copyright 2019 Springer Nature. (b) Schematic diagram of the interfacial transport challenges in lithium metal solid-state batteries. Lithium metal undergoes oxidation and migrates as Li^+ to the solid electrolyte leaving an electron and a vacancy in the lithium metal. During stripping at high current densities, the vacancies formed due to Li^+ migration accumulate faster than can be replenished by self-diffusion of Li metal. This results in formation of voids at the anodelSE interface. On subsequent cycling, the void acts as focusing regions for nonplanar Li deposition. (c) Sample reconstruction slices of lithium metal electrode imaged for pristine, plating, and stripping steps. Semicircular morphologies are observed in the plating as well as stripping electrode, and pore formation in the stripping electrode is observed. (d) Segmentation from the conventional binarization process overlaid with raw reconstruction images. Darker regions in these images are identified pores/void phase while the lighter domains are lithium metal. (e) Segmentation results from convolutional neural networks overlaid with raw reconstruction images. The green phase is the identified lithium metal while the blue phase is the identified pore/void phases.

observations (Figure 1a), there are no in situ experimental observations that track pore evolution dynamics and gradients within lithium metal electrodes.

High-resolution imaging of lithium metal at buried solidl solid interfaces is challenging because low atomic number elements weakly interact with experimental probes. Additionally, for in situ and operando imaging, proximity to highly absorbing/scattering materials (steel current collector, LLZO electrolyte) significantly impedes extracting morphological information from lithium metal. Maintaining a stable, air-free environment during operation is also a key experimental challenge. Filament formation is typically characterized by ex situ optical/electron microscopy due to these experimental challenges.[20,21] Recent operando optical imaging of LilLLZOl Li systems demonstrated how the morphology of the filament differed depending on the operating regime (e.g., current density) which suggests that there are a variety of failure mechanisms.[9] While microscopy and optical imaging offer valuable material insights, it is challenging to resolve dynamic material processes that occur in subsurface and bulk materials. Synchrotron X-ray tomography (XRT) is a potential method to resolve three-dimensional morphological transformations with adequate spatial and temporal resolutions relevant to solid-state batteries.[4,22] Recently, XRT was used to track morphological variation in Na metal anodes during cycling which showed clear evidence of a pore formation mechanism.[15] There is some literature that leverages synchrotron imaging to evaluate transformations in lithium metal,[4,23,24] but the reported studies use low-density systems (graphite, polymer) in combination with lithium metal. Enabling lithium metal visualization by synchrotron imaging in combination with a high-density solid electrolytes (LLZO) has not been previously reported.

This work uses imaging techniques to track morphological transformations at lithium metallsolid electrolyte interfaces. A garnet (LLZO) solid electrolyte is chosen as the model electrolyte to image because it is one of the most stable solid electrolytes, and it has minimal interphase formation. In order to process the low-contrast images (lithium metal and pores), advanced image processing and machine learning methods were developed for effective segmentation to extract quantitative metrics of the electrodes (current density, porosity, and their spatial distribution) during cycling (Figure 1c–e). Furthermore, in situ experiments allow for tracking Li metal morphological transformations at stripping and plating electrodes simultaneously. Advanced visualization combined with electrochemistry represents an important pathway toward resolving the role non-equilibrium defects, and microstructure heterogenities impact rate capabilities of lithium metal anodes. Spatial variations in microstructrural properties of the solid electrolyte are correlated to the hot spot generation within the lithium metal (Figure 1a). Mesoscale simulations of the solid electrolyte reveal heterogeneous transport and mechanical properties. Failure onset at LilSE interfaces occurs at regions with lower transport and mechanical properties.

X-ray imaging relies on absorption and phase contrast to distinguish materials in the field-of-view of the beam. Absorption contrast captures differences in the attenuation of the X-rays along the trajectory from the source to the detector. The attenuation depends on the spatial density of the material,

https://dx.doi.org/10.1021/acsaem.0c02053
ACS Appl. Energy Mater. 2020, 3, 9534−9542

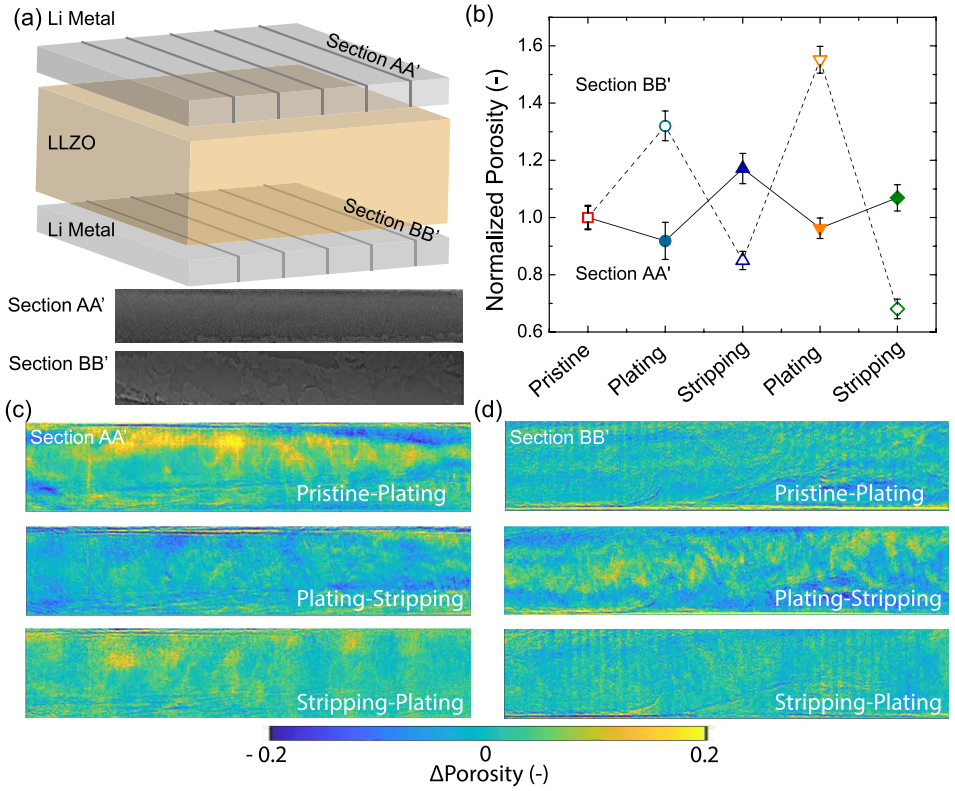

Figure 2. (a) Schematic diagram showing sections imaged from the two lithium metal electrodes in the Li|LLZO|Li system. Pore density difference maps are evaluated by averaging over a transverse thickness of approximately 500 μm. (b) Porosity variation of a single electrode at subsequent electrochemical cycling stages. This porosity is estimated near the solid electrolyte interface. This quantification is carried out on segmented Li metal images obtained from the convolutional neural network. Spatial pore density difference distribution for the (c) top and (d) bottom electrodes at various electrochemical cycling stages. Identical preprocessing, segmentation, and postprocessing steps are employed for all the individual data sets to enable comparison.

the depth of the sample, and the incident X-ray wavelength. Assuming there is one material in the X-ray beam, this attenuation is described by the Beer−Lambert law:

$$I(x, y, \lambda) = I_0(x, y)\exp[-(\mu_0^{\lambda} - \mu_h^{\lambda})T_0(x, y)] \quad (1)$$

where I is the attenuated intensity, I_0 is the incident intensity, μ_0^{λ} is the attenuation coefficient of air, μ_h^{λ} is the attenuation coefficient of sample for X-rays of wavelength λ, and T_0 is the projected thickness through point (x, y) in the direction of z, which is the propagation direction of the X-ray beam. In addition to attenuation, X-rays will undergo a phase shift after traversing a material. The phase shift is determined by the real part of the complex refractive index of the material which depends on the incident X-ray wavelength and local electron density. The phase shift imparted by the sample to the X-ray is given by[25]

$$\Phi(x, y, \lambda) = -k\int_O \mathrm{d}z\, \delta(x, y, z, \lambda) \quad (2)$$

where Φ is the phase shift, δ is the real part of the complex refractive index (in terms of $n = 1 - \delta + i\beta$), k is a proportionality constant, and the integration is carried out over the extent of object O along the optical axis. While it is not possible to directly measure the phase of the transmitted X-rays, the interference pattern is captured and reconstructed. The phase contrast is enhanced specifically at the interfaces between materials. Distinguishing low-density phases (pores, lithium metal) is challenging for larger sample sizes as well as without adequate phase contrast. The careful combination of absorption and phase contrast and experimental design enables lithium metal imaging at buried solid|solid interfaces. Monochromatic, high-energy X-rays (E = 76.2 keV) are employed for imaging the Li|LLZO|Li system. High monochromaticity ($\Delta E/E \approx 10^{-3}$) allows us to distinguish low-density phases (voids/Li metal). The transverse sample thickness was reduced to about 1.5 mm to match the field-of-view. The sample−detector distance was selected to ensure optimum phase contrast. A GRIDREC reconstruction algorithm was used to ensure high-quality reconstructions.[26] Reconstruction across different electrochemical steps shows marked differences in the lithium metal electrode (Figure 1d and Figures S1 and S2). Optimized experimental and reconstruction protocols enable visualizing the morphology variation in lithium metal as well as the presence of pores within the electrode. Semicircular domains (Figure 1c) are visualized in lithium metal on plating as well as stripping. This morphology closely resembles lithium ion flux profiles around a hot spot at the electrodelelectrolyte interface (Figure S3). Such deposition morphologies were postulated in an earlier study.[27] This is the first mesoscale experimental observation of such morphologies in lithium metal electrodes at solid electrolyte interfaces. Stripping from the same electrode leads to formation of a similar semicircular feature with the presence of voids (darker regions) near the interface (Figure 1d). Regions in the center of a stripping hot spot would have higher mass flux leaving the domain leading to the generation of voids due to a flux imbalance.

https://dx.doi.org/10.1021/acsaem.0c02053
ACS Appl. Energy Mater. 2020, 3, 9534−9542

Quantification of microstructural properties (pores/voids) in the lithium electrode requires a rigorous and consistent segmentation procedure. Conventional thresholding methods cannot segment the phases (pores vs lithium) reliably (Figure 1c), and manual segmentation of the entire data set is prohibitive. The convolutional neural network is a machine learning method widely used for semantic segmentation in a wide range of disciplines that enable pixel-level classification of large data sets. We implemented a resnet34 based deep convolution neural network for enabling lithium metal segmentation. The neural network processed individual cross-sectional images of lithium metal to yield a high-confidence segmented image (Figure 1e). Improvement in fidelity and accuracy of void phase identification for the machine learned segmentation is apparent in comparison to the conventional binarization process. Conventional binarization identifies a significant number of pixels as pores in the pristine sample, which are wrongly segmented while missing several, significant pore features in the stripping electrode. These images clearly highlight the importance of combining synchrotron XRT with machine learning methods to effectively track transformations within the lithium metal anode. Machine learning methods required approximately 0.3 s for individual slice segmentation, with greater than 80% confidence (Figure S4). The segmentation times are an order of magnitude smaller than those typically needed for manual labeling of these images while the confidence statistics are competitive with the segmentation confidence obtained by state-of-the-art networks on standard data sets.[28] The neural network was trained on 800 images from one electrode in a single electrochemical cycle and validated on an additional 200 additional images from the same electrode. Training and validation labeled images were generated by computationally edge-segmented and manually corrected images. The quantification metrics discussed are obtained from the segmented images obtained by applying the trained network to all the subsequent data sets. It should be noted that the segmentation introduces some error in quantification (80% confidence). Absolute quantification is not advised; however, relative trends between successive electrochemical steps can be ascertained. Preprocessing, segmentation, and postprocessing steps are identical for all the evaluated data sets enabling a comparative evaluation.

The complete Li|LLZO|Li cell is imaged in a single scan allowing for simultaneous tracking of both the deposition and the dissolution electrodes (Figure 2a). This is crucial for identifying key differences in morphological evolution and corresponding kinetics at the two electrodes simultaneously. Cross-sectional images of the lithium metal electrodes are cropped out from the reconstructions as identified for both electrodes (Figure 2a). A spatial pore density distribution is evaluated by averaging over a 500 μm depth of lithium metal electrode of such sections. The differences in the spatial pore density between successive electrochemical steps are visualized for the top and bottom electrodes (Figure 2c,d). Both electrodes show a highly heterogeneous distribution of the porosity change, spatially suggesting that the interfacial kinetics are highly nonuniform. Additionally, the two electrodes show complementary behaviors of porosity differences consistent with the electrochemical phenomena occurring at the two electrodes. A mass transport imbalance at the Li|SE interface is widely postulated to generate voids at the interface in solid-state batteries.[16,27] So far, limited cross-sectional imaging evidence is provided for this mechanism.[16] In situ tomography configured specifically to track lithium metal enables quantitative assessment of this phenomena. Higher mass flux at the interface due to high local current density, inadequate metal diffusion and creep flow can lead to generation of these voids. Normalized porosity measured near the interface (10 μm) clearly reflects this phenomenological model proposed, with plating showing a reduction in porosity and stripping leading to an increase in porosity in the lithium metal (Figure 2b). Further, the importance of the developed convolutional neural network in discerning the pore features in lithium metal is investigated by the quantification of porosity of binarized Li metal images. The Otsu thresholding algorithm was employed for thresholding, and the results show no trends during cycling (Figure S14). Comparing the quantification results from the two methods (binarization, CNN) clearly showcases the usefulness of advanced ML methods in discerning pores from Li metal.

This behavior is also reflected over the entire electrode section as well with porosity increases from the plating step to the stripping step (Figure S5a). Pristine lithium metal demonstrates a single modal porosity probability distribution while the plated and stripped samples have a nonuniform (trimodal) distribution. The trimodal distribution indicates larger spatial variation (variance) within the electrode section introduced due to electrochemical cycling. Additionally, the pore distribution along the electrode depth can be visualized using the segmented data (Figure S5b). Individual data points in this graph are obtained by averaging the porosity over a 10 μm thickness. The porosity at the Li|SE is greater than in the bulk metal regions. The high porosity at the interface suggests the formation of voids and interfacial delamination. Electrochemical cycling induced changes in the porosity depth profile are identified closer to the solid electrolyte interface. Porosity values at the current collector are consistent across the electrochemical steps suggesting that this region does not undergo active morphological changes during cycling. These results match well with the anticipated flux profiles in the vicinity of interfacial hot spots (Figure S3c) wherein flux gradients are concentrated near the solid electrolyte interface with less impact of the hot spot near the current collector end. Such behavior is only expected in systems with a thick lithium foil electrode (higher excess lithium). As we examine systems with limited or no excess lithium, morphological changes are expected to propagate through the entire bulk of lithium metal. These morphological characterizations of bulk lithium metal are made possible due to the careful experimental design and the developed machine learning segmentation methods. Synchrotron XRT coupled with machine learning methods is likely to prove to be an essential tool for assessing and decoupling the effects of microstructure, operating conditions, and interfacial kinetics on the lithium metal anode.

A critical current density of approximately 26 μA cm^{-2} was identified from the in situ experiments (Figure S6). It is important to note here that enabling Li metal visualization for in situ conditions by synchrotron XRT is extremely challenging due to the limitations in terms of sample size, environment, and operating parameters. A brief summary of literature reveals a large variance in the reported critical current densities ranging from several μA cm^{-2} to mA cm^{-2} (Figure S13). The latter are generally reported at high stack pressures and elevated temperatures. Additionally, several studies also employ interlayers at the Li|LLZO interface (ZnO, Al_2O_3, Au) to enable a high critical current density. The metrics

https://dx.doi.org/10.1021/acsaem.0c02053
ACS Appl. Energy Mater. 2020, 3, 9534−9542

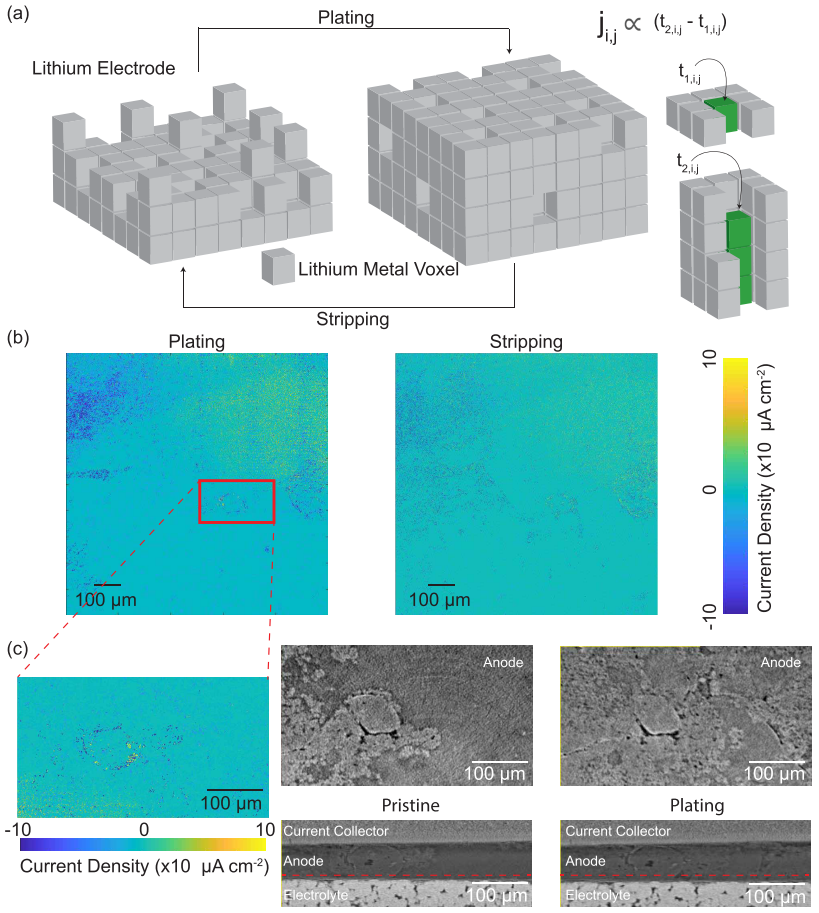

Figure 3. (a) Schematic diagram describing the current density quantification method. Differences in lithium electrode thickness are evaluated at each location across the electrode area. The local current density is proportional to the difference of the thickness of lithium electrode in successive image sets. (b) Current density maps for plating and stripping steps of a single electrode. (c) Expanded region identified as the region possessing potential hot spots, and the corresponding sectional images are from the raw tomography data. Regions with uniform current density show evidence of planar deposition, while the locations with lower current density directly correlate to the presence of pores/voids within the electrode. Additionally, differences in the subsurface electrolyte microstructre in these sections are clearly visible.

reported in this study arise from a model Li|LLZO|Li system run at a significantly lower stack (kPa range) and the challenge of assembling a cell at the relevant physical dimensions (1.5 mm diameter). Achieving the operating conditions reported for the high critical current density requires an extensive experimental setup that is harder to couple with an in situ cell compatible with the beamline endstation. Interfacial resistances (≈2000 Ω cm^{-2}) observed here are consistent with the reports for lower stack pressure systems. Further, low initial polarization is comparable to previous ex situ measurements[3] and indicates an effective Li|LLZO|Li system for the characterization study. Thus, the results described here are characteristic transformations of lithium metal and solid electrolyte interface.

An in situ tomography data set can generally be large in size particularly if the sample is large and many electrochemical steps are probed. A typical tomography scan of a symmetric cell results in a data set greater than 30 GB. Tracking pixel-level changes in morphology of lithium metal across these data sets is prohibitive. An analytical approach was developed to enable faster analysis via finding regions of interest (Figure 3a). Regions of interest are considered the location where either pores form in lithium metal, delamination may occur, and/or nucleation sites are present for filament formation. To identify these regions of interest, we quantified a spatial current density profile across the lithium metal. This can be estimated by tracking the thickness of the electrode over different electrochemical steps given as[22]

$$j_{i,j} = \frac{(t_{2,i,j} - t_{1,i,j})F}{\Delta t V_{\mathrm{Li}}} \tag{3}$$

where $j_{i,j}$ is the spatial current density at a location specified by coordinates i and j, $t_{2,i,j}$ and $t_{1,i,j}$ are the thicknesses of a lithium metal electrode at steps 1 and 2, F is Faraday's constant, Δt is the time duration of electrochemical cycle, and V_{Li} is the molar volume of lithium. The thickness of the lithium metal electrode was estimated by measuring intensity line profiles at each location through the depth of the sample. Distinct absorption contrast between steel (current collector) and the LLZO electrolyte enables identification of the electrode thickness. This measurement can be easily automated enabling faster tracking of the data sets by providing qualitative information for easier identification of hot spots. Specifically, with the current data set, mapping the current density over a 1 mm^2 area for both electrodes in a symmetric cell takes ≈20 min. Spatial current density maps for the plating and stripping cycle show a significant variation (Figure 3b). Most of the lithium metal shows a uniform current density and is denoted by green/blue (Figure 3b,c). There are isolated spots that demonstrate either a greater than average current density

https://dx.doi.org/10.1021/acsaem.0c02053
ACS Appl. Energy Mater. 2020, 3, 9534−9542

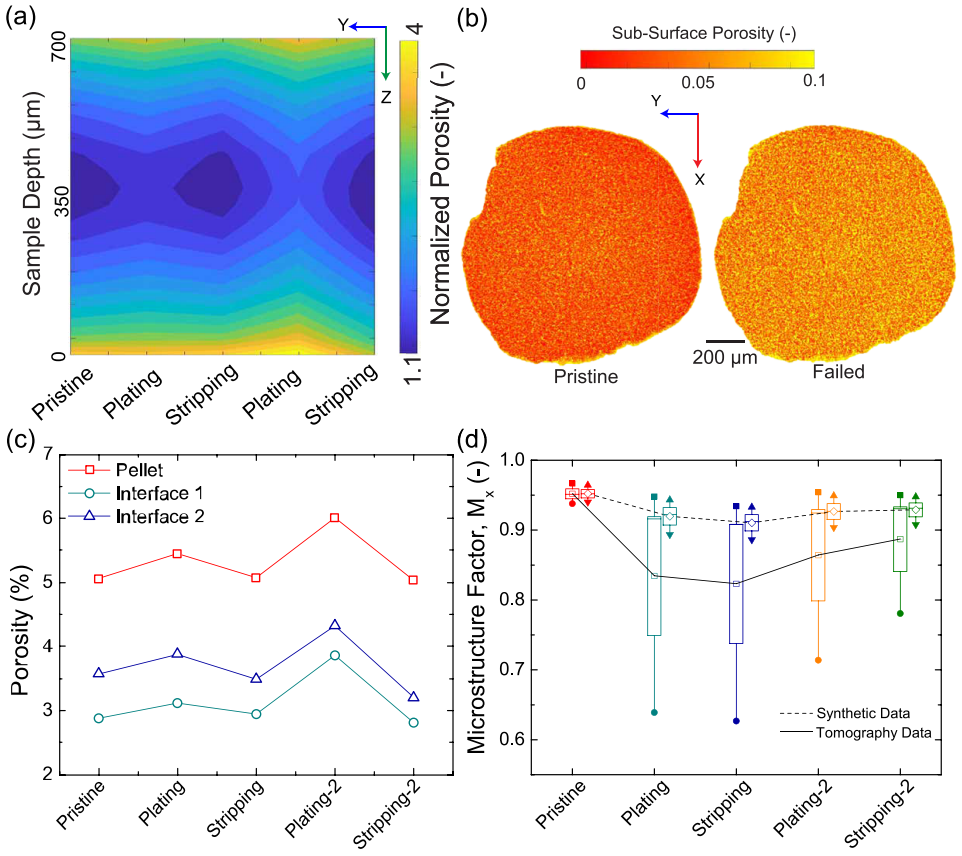

Figure 4. (a) Spatial microstructural variation within the sample evaluated across multiple electrochemical cycling steps. Normalized porosity is plotted which is defined as the ratio of the local porosity to the average electrolyte porosity. Spatial resolution of 36 μm was used to assess the microstructural variation through the depth of the electrolyte. (b) Subsurface porosity map measured through the depth of the sample for the pristine and the failed electrolyte pellet. (c) Bulk pellet porosity and interfacial porosity evaluated across each cycling step. Interfacial regions of 100 μm are considered for this analysis to correlate with the results obtained from the tortuosity factor calculations. (d) Microstructure factor (ratio of local property/bulk property) estimated along the *X* direction (along Li|SE|Li) of the domain from the tomography and synthetic data set. The tomography data set uses the binarized reconstruction images as input for the simulations, while the synthetic data set uses isotropic domains generated from the quantified physical parameters.

(yellow) or a lower than average current density (blue). A potential hot spot region (yellow) is identified from the current density plots for further analysis of the raw projections (Figure 3c). A comparison of pristine and plating morphologies of the identified section shows the presence of interfacial pores as well as globular depositions. In addition to different plating morphologies, a clear difference in the electrolyte microstructure is observed for the hot spot region identified. Analysis of additional hot spot regions across multiple cycles shows consistent results (Figures S7 and S8). Spatial current density mapping aids in identifying local hot spots. Combining spatial current density mapping with imaging allows for directly tracking meso- and microstuctural properties that may impact the formation of hot spots while reducing the analysis time and computational power required for assessment of in situ tomography data.

Morphological changes captured in the lithium metal are intimately linked to the underlying solid electrolyte and the Li| SE interface. Understanding and evaluating the transformations in the electrolyte microstructure can help in identifying the origins of morphological transformations observed in the lithium metal electrode. The average porosity of the pristine pellet was ≈5%, indicating well-sintered, dense pellets. Normalized porosity shows a cyclic behavior with electrochemical cycles which decreases on plating and increases on stripping (Figure 4a). The nominally X-ray transparent region (generically porosity) includes pores and voids as well as lithium deposition, as these materials are difficult to distinguish within the bulk electrolyte. Modulation within this region can be interpreted as the presence of electrochemically active lithium metal within the bulk electrolyte. The normalized pore density depth profile also shows spatial variation within the electrolyte domain with interfaces being more porous compared to the bulk. Higher amounts of the X-ray transparent region at the interfaces can arise from crack/void generation from the mechanical stresses at the interface as well as from filament generation. Increasing the current density from 6 to 25 μA cm^{-2} on second plating/stripping cycles leads to greater penetration of the higher-porosity regions into the bulk. This can reflect potential filament/crack propagation within the bulk. The spatial distribution is practically symmetric across the electrolyte depth suggesting identical mechanisms at both the plating and stripping electrodes. While the lithium metal electrode undergoes distinct morphological changes (void formation on stripping, nonplanar deposition on plating), the nominally identical response of the LLZO electrolyte interfaces suggest they are influenced by the same underlying mechanics. Ion transport to and removal from the LLZO matrix at the interfaces causes stress generation within the solid electrolyte material. These phenomena lead to

https://dx.doi.org/10.1021/acsaem.0c02053
ACS Appl. Energy Mater. 2020, 3, 9534−9542

microstructural variations as evidenced by the tomography results. Further work on evaluating the spatially resolved, grain-level chemomechanical response is required to understand the identical mechanical behavior at plating and stripping interfaces.

Subsurface porosity maps reflect the porosity averaged through the Z direction (sample depth) at each pixel along the lateral (XY) section. The solid electrolyte shows a systematic increase in the subsurface porosity consistent with the mechanism of filament propagation (Figure 4b and Figure S9).[3] The location and size of the X-ray transparent region (porosity) across the pellet as well as in the interfacial regions show a cyclic behavior with electrochemical steps (Figure 4c and Figure S9). Average porosity clearly reflects a difference in the microstructure between successive electrochemical steps in the interfacial regions which is effectively captured in the simulations. It is known that single ion conductors theoretically do not show concentration gradients due to the unity transference numbers. However, the presence of pores has been identified to strongly influence transport and failure mechanisms.[3,29] The subsurface porosity maps clearly highlight the spatial microstructural variation, specifically at the interfacial regions. Additionally, tortuosity factors are extracted in the bulk and interfacial region of the solid electrolyte. Tortuosity factors are determined along the Z direction which coincides with the electric field direction in the cell (Figure S10a). Normalized tortuosity shown here is the relative change in local tortuosity factor compared to a completely solid domain (tortuosity factor = 1). This metric reflects the degree of obstruction the ions experience when traversing through the solid electrolyte. High-tortuosity regions lead to a lower effective lithium ion flux through the domain as given by[30]

$$\rho_{\text{eff}} = -D_{\text{bulk}} \frac{\epsilon}{\tau^2} \frac{\Delta c}{\Delta x} \tag{4}$$

where D_{bulk} is the effective diffusion coefficient in the bulk, ϵ is the porosity, τ is the tortuosity, and $\frac{\Delta c}{\Delta x}$ is the effective concentration gradient. Regions of lower tortuosity surrounded by high-tortuosity domains correspond to hot spots as lithium ion flux through the low-tortuosity domains will be higher to ensure mass balance through the cell section. Variations in tortuosity factors in the sample at individual plating and stripping steps indicate a strong heterogeneity in the underlying microstructure (Figure S11). Tortuosity factor maps provide evidence for transport heterogeneity due to the underlying microstructure variations. Hot spot generation leading to void and filament formation within the lithium metal electrode is linked with the microstructural heterogeneity identified in the solid electrolyte.

To further ascertain the influence of the spatial heterogeneity, mesoscale modeling was carried out for representative simulation domains from the interfacial region of the LLZO electrolyte. Two data set formulations were used: (a) tomography data which employed the imaged domain directly and (b) synthetic data which employed isotropic domains generated from physical parameters (porosity, pore size, and grain size) identified from the experimental results. Mesoscale modeling enables explicit definitions of grains, pores, as well as grain boundaries to ascertain effective bulk properties of materials (Figure S10b). The microstructure factor (M_x, M_y, and M_z) is defined as the ratio of the local conductivity/Young's modulus estimated along the X, Y, and Z direction in the simulated domain to the theoretical value for LLZO. Mean, maximum, and minimum microstructure factors have been calculated during electrochemical cycling for both the synthetic and experimental data sets. A strong impact of sample microstructure anisotropy is seen in the tomography data set with X direction showing a markedly higher variation across different electrochemical steps in microstructure factor compared to the Y and Z directions (Figure 4d and Figure S12). In contrast, the synthetic data (isotropic domains) show only a small variation linked to the changes in the effective microstructure. Additionally, the tomography domains show a higher spread (minimum, maximum) compared to the isotropic domains signifying a large heterogeneity in local transport and mechanical properties. Identical behavior is seen for the for multiple Li|LLZO systems studied, with comparatively lower anisotropy related fluctuations (variations along X, Y, and Z direction). These results clearly show that macroscopic properties of conductivity and Young's modulus are affected by microstructural heterogeneity. Higher plating density is anticipated in regions around the domains showing lower transport properties to ensure mass balance across the interface. High plating density around these regions leads to stress accumulation which can subsequently lead to cracking/filament propagation through the electrolyte at the regions with the lower effective properties. The investigation of electrolyte microstructure yields strong evidence for origins of the heterogeneous current density observed in the lithium metal electrodes. Microstructural variation in the solid electrolyte leads to regions with lower transport and mechanical properties that can act as nucleation sites for hot/cold spots at the Li|SE interface.

Careful experimental design enables high-resolution X-ray imaging of lithium metal. Advanced machine learning methods enable segmentation of lithium and pores from the reconstructions of in situ conditions. This data provides physical insight into microstructure transformation in lithium metal and the solid electrolyte upon cycling. Heterogeneous interfacial kinetics are identified in lithium metal along with a validation of pore formation hypothesis on dissolution. Hot spots in lithium metal electrodes are correlated with the presence of anisotropic microstructures within the solid electrolyte. Mesoscale modeling results conclusively show local variations in effective properties of the electrolyte at the electrode interface. Local domains showing lower effective properties are construed to be regions where failure modes are initiated due to stress and flux distributions around these regions. Lithium metal electrode kinetics at solid electrolyte interfaces are distinct from liquid electrolytes. The imaging resolution and contrast described here lay the groundwork for future studies capable of resolving the role of microstructure heterogeneities in lithium metal which impact electrodeposition stability and rate performance.

■ ASSOCIATED CONTENT

Supporting Information

The Supporting Information is available free of charge at https://pubs.acs.org/doi/10.1021/acsaem.0c02053.

Detailed experimental methods, modeling framework description, and additional figures for statistics (PDF)

https://dx.doi.org/10.1021/acsaem.0c02053
ACS Appl. Energy Mater. 2020, 3, 9534−9542

AUTHOR INFORMATION

Corresponding Author

Kelsey B. Hatzell − *Department of Mechanical Engineering, Chemical and Biomolecular Engineering, and Interdisciplinary Material Science Program, Vanderbilt University, Nashville, Tennessee 37240, United States;* orcid.org/0000-0002-5222-7288; Phone: +1 (615)-875-8391; Email: kelsey.b.hatzell@vanderbilt.edu

Authors

Marm B. Dixit − *Department of Mechanical Engineering, Vanderbilt University, Nashville, Tennessee 37240, United States;* orcid.org/0000-0002-9599-9288

Ankit Verma − *School of Mechanical Engineering, Purdue University, West Lafayette, Indiana 47907, United States*

Wahid Zaman − *Department of Mechanical Engineering, Vanderbilt University, Nashville, Tennessee 37240, United States*

Xinlin Zhong − *Department of Mechanical Engineering, Vanderbilt University, Nashville, Tennessee 37240, United States*

Peter Kenesei − *X-ray Science Division, Advanced Photon Source, Argonne National Laboratory, Lemont, Illinois 60439, United States*

Jun Sang Park − *X-ray Science Division, Advanced Photon Source, Argonne National Laboratory, Lemont, Illinois 60439, United States*

Jonathan Almer − *X-ray Science Division, Advanced Photon Source, Argonne National Laboratory, Lemont, Illinois 60439, United States*

Partha P. Mukherjee − *School of Mechanical Engineering, Purdue University, West Lafayette, Indiana 47907, United States*

Complete contact information is available at: https://pubs.acs.org/10.1021/acsaem.0c02053

Notes

The authors declare no competing financial interest.

The submitted manuscript has been created by UChicago Argonne, LLC, Operator of Argonne National Laboratory ("Argonne"). Argonne, a U.S. Department of Energy Office of Science laboratory, is operated under Contract DE-AC02-06CH11357. The U.S. Government retains for itself, and others acting on its behalf, a paid-up nonexclusive, irrevocable worldwide license in said article to reproduce, prepare derivative works, distribute copies to the public, and perform publicly and display publicly, by or on behalf of the Government. The Department of Energy will provide public access to these results of federally sponsored research in accordance with the DOE Public Access Plan. http://energy.gov/downloads/doe-public-access-plan.

ACKNOWLEDGMENTS

K.B.H. and M.B.D. acknowledge support from National Science Foundation Grant 1847029. K.B.H. and W.Z. acknowledge support from from National Science Foundation Grant 1821573. P.P.M. and A.V. acknowledge financial support in part from a Scialog program sponsored jointly by Research Corporation for Science Advancement and the Alfred P. Sloan Foundation which includes a grant to Purdue University by the Alfred P. Sloan Foundation. The authors acknowledge the Vanderbilt Institute of Nanoscience and Engineering (VINSE) for access to their shared characterization facilities. This research used resources of the Advanced Photon Source, a U.S. Department of Energy (DOE) Office of Science User Facility operated for the DOE Office of Science by Argonne National Laboratory under Contract DE-AC02-06CH11357.

REFERENCES

(1) Hatzell, K. B.; Chen, X. C.; Cobb, C.; Dasgupta, N. P.; Dixit, M. B.; Marbella, L. E.; McDowell, M. T.; Mukherjee, P.; Verma, A.; Viswanathan, V.; Westover, A.; Zeier, W. G. Challenges in Lithium Metal Anodes for Solid State Batteries. *ACS Energy Lett.* **2020**, *5*, 922−934.

(2) Monroe, C.; Newman, J. Dendrite Growth in Lithium/Polymer Systems A Propagation Model for Liquid Electrolytes Under Galvanostatic Conditions. *J. Electrochem. Soc.* **2003**, *150*, A1377−A1384.

(3) Shen, F.; Dixit, M.; Xiao, X.; Hatzell, K. The Effect of Pore Connectivity on Li Dendrite Propagation Within LLZO Electrolytes Observed with Synchrotron X-ray Tomography. *ACS Energy Lett.* **2018**, *3*, 1056−1061.

(4) Harry, K. J.; Hallinan, D. T.; Parkinson, D. Y.; MacDowell, A. A.; Balsara, N. P. Detection of Subsurface Structures Underneath Dendrites Formed on Cycled Lithium Metal Electrodes. *Nat. Mater.* **2014**, *13*, 69−73.

(5) Wang, M. J.; Choudhury, R.; Sakamoto, J. Characterizing the Li-Solid-Electrolyte Interface Dynamics as a Function of Stack Pressure and Current Density. *Joule* **2019**, *3*, 2165−2178.

(6) Zhang, X.; Wang, Q. J.; Harrison, K. L.; Roberts, S. A.; Harris, S. J. Pressure-Driven Interface Evolution in Solid-State Lithium Metal Batteries. *Cell Rep. Phys. Sci.* **2020**, *1*, 100012.

(7) Chang, H. J.; Trease, N. M.; Ilott, A. J.; Zeng, D.; Du, L.-S.; Jerschow, A.; Grey, C. P. Investigating Li microstructure formation on Li anodes for lithium batteries by in situ ^{6}Li/^{7}Li NMR and SEM. *J. Phys. Chem. C* **2015**, *119*, 16443−16451.

(8) Schmalzried, H.; Janek, J. Chemical Kinetics of Phase Boundaries in Solids. *Ber. Bunsmges. Phys. Chem.* **1998**, *102*, 127−143.

(9) Kazyak, E.; Garcia-Mendez, R.; LePage, W. S.; Sharafi, A.; Davis, A. L.; Sanchez, A. J.; Chen, K. H.; Haslam, C.; Sakamoto, J.; Dasgupta, N. P. Li Penetration in Ceramic Solid Electrolytes: Operando Microscopy Analysis of Morphology, Propagation, and Reversibility. *Matter* **2020**, *2*, 1025−1048.

(10) Dixit, M. B.; Zaman, W.; Hortance, N.; Vujic, S.; Harkey, B.; Shen, F.; Tsai, W.-Y.; De Andrade, V.; Chen, X. C.; Balke, N.; Hatzell, K. B. Nanoscale mapping of extrinsic interfaces in hybrid solid electrolytes. *ACS Appl. Mater. Interfaces* **2020**, *4* (1), 207−221.

(11) Fu, C.; Venturi, V.; Kim, J.; Ahmad, Z.; Ells, A. W.; Viswanathan, V.; Helms, B. A. Universal Chemomechanical Design Rules for Solid-Ion Conductors to Prevent Dendrite Formation in Lithium Metal Batteries. *Nat. Mater.* **2020**, *19*, 758−766.

(12) Mistry, A.; Mukherjee, P. P. Molar Volume Mismatch: a Malefactor for Irregular Metallic Electrodeposition with Solid Electrolytes. *J. Electrochem. Soc.* **2020**, *167*, 082510.

(13) Yonemoto, F.; Nishimura, A.; Motoyama, M.; Tsuchimine, N.; Kobayashi, S.; Iriyama, Y. Temperature Effects on Cycling Stability of Li Plating/Stripping on Ta-Doped $Li_7La_3Zr_2O_{12}$. *J. Power Sources* **2017**, *343*, 207−215.

(14) Krauskopf, T.; Dippel, R.; Hartmann, H.; Peppler, K.; Mogwitz, B.; Richter, F. H.; Zeier, W. G.; Janek, J. Lithium-Metal Growth Kinetics on LLZO Garnet-Type Solid Electrolytes. *Joule* **2019**, *3*, 2030−2049.

(15) Spencer Jolly, D.; Ning, Z.; Darnbrough, J. E.; Kasemchainan, J.; Hartley, G. O.; Adamson, P.; Armstrong, D. E.; Marrow, J.; Bruce, P. G. Sodium/Na β'' Alumina Interface: Effect of Pressure on Voids. *ACS Appl. Mater. Interfaces* **2020**, *12*, 678−685.

(16) Kasemchainan, J.; Zekoll, S.; Spencer Jolly, D.; Ning, Z.; Hartley, G. O.; Marrow, T. J.; Bruce, P. G. Critical Stripping Current Leads to Dendrite Formation on Plating in Lithium Anode Solid Electrolyte Cells. *Nat. Mater.* **2019**, *18*, 1105−1111.

(17) Hiratani, M.; Miyauchi, K.; Kudo, T. Effect of a Lithium Alloy Layer Inserted Between a Lithium Anode and a Solid Electrolyte. *Solid State Ionics* **1988**, *28*−*30*, 1406−1410.
(18) Schlenker, R.; Stępień, D.; Koch, P.; Hupfer, T.; Indris, S.; Roling, B.; Miß, V.; Fuchs, A.; Wilhelmi, M.; Ehrenberg, H. Understanding the Lifetime of Battery Cells Based on Solid-State Li_6PS_5Cl Electrolyte Paired with Lithium Metal Electrode. *ACS Appl. Mater. Interfaces* **2020**, *12*, 20012−20025.
(19) Jow, T.; Liang, C. Interface Between Solid Electrode and Solid Electrolyte—A Study of the Li/LiI (Al_2O_3) Solid-Electrolyte System. *J. Electrochem. Soc.* **1983**, *130*, 737.
(20) Lewis, J. A.; Cortes, F. J. Q.; Boebinger, M. G.; Tippens, J.; Marchese, T. S.; Kondekar, N.; Liu, X.; Chi, M.; McDowell, M. T. Interphase Morphology between a Solid-State Electrolyte and Lithium Controls Cell Failure. *ACS Energy Lett.* **2019**, *4*, 591−599.
(21) Porz, L.; Swamy, T.; Sheldon, B. W.; Rettenwander, D.; Frömling, T.; Thaman, H. L.; Berendts, S.; Uecker, R.; Carter, W. C.; Chiang, Y. Mechanism of Lithium Metal Penetration Through Inorganic Solid Electrolytes. *Adv. Energy Mater.* **2017**, *7*, 1701003.
(22) Maslyn, J. A.; Frenck, L.; Loo, W. S.; Parkinson, D. Y.; Balsara, N. P. Extended Cycling Through Rigid Block Copolymer Electrolytes Enabled by Reducing Impurities in Lithium Metal Electrodes. *ACS Appl. Energy Mater.* **2019**, *2*, 8197−8206.
(23) Adair, K. R.; Banis, M. N.; Zhao, Y.; Bond, T.; Li, R.; Sun, X. Temperature-Dependent Chemical and Physical Microstructure of Li Metal Anodes Revealed through Synchrotron-Based Imaging Techniques. *Adv. Mater.* **2020**, *32*, 2002550.
(24) Taiwo, O. O.; Finegan, D. P.; Paz-Garcia, J. M.; Eastwood, D. S.; Bodey, A. J.; Rau, C.; Hall, S. A.; Brett, D. J.; Lee, P. D.; Shearing, P. R. Investigating the Evolving Microstructure of Lithium Metal Electrodes in 3D Using X-Ray Computed Tomography. *Phys. Chem. Chem. Phys.* **2017**, *19*, 22111−22120.
(25) Endrizzi, M. X-ray Phase-Contrast Imaging. *Nucl. Instrum. Methods Phys. Res., Sect. A* **2018**, *878*, 88−98.
(26) Dowd, B. A.; Campbell, G. H.; Marr, R. B.; Nagarkar, V. V.; Tipnis, S. V.; Axe, L.; Siddons, D. P. Developments in Synchrotron X-ray Computed Microtomography at the National Synchrotron Light Source. *Proc. SPIE* **1999**, 224−236.
(27) Wang, M.; Wolfenstine, J. B.; Sakamoto, J. Temperature Dependent Flux Balance of the $Li/Li_7La_3Zr_2O_{12}$ Interface. *Electrochim. Acta* **2019**, *296*, 842−847.
(28) Zhang, Y.; Yu, H. Convolutional Neural Network Based Metal Artifact Reduction in X-Ray Computed Tomography. *IEEE Trans. Med. Imaging* **2018**, *37*, 1370−1381.
(29) Dixit, M. B.; Regala, M.; Shen, F.; Xiao, X.; Hatzell, K. B. Tortuosity Effects in Garnet-Type $Li_7La_3Zr_2O_{12}$ Solid Electrolytes. *ACS Appl. Mater. Interfaces* **2019**, *11*, 2022−2030.
(30) Tjaden, B.; Brett, D. J.; Shearing, P. R. Tortuosity in Electrochemical Devices: A Review of Calculation Approaches. *Int. Mater. Rev.* **2018**, *63*, 47−67.
(31) Krauskopf, T.; Hartmann, H.; Zeier, W. G.; Janek, J. *ACS Appl. Mater. Interfaces* **2019**, *11*, 14463.

https://dx.doi.org/10.1021/acsaem.0c02053
ACS Appl. Energy Mater. 2020, 3, 9534−9542